



Research paper

Optical modeling, solver, and design of macroscopic single-enantiomer carbon nanotube film and reconfigurable chiral photonic device

Jichao Fan^a, Benjamin Hillam^a, Cheng Guo^b, Hiroyuki Fujinami^c, Koki Shiba^c, Haoyu Xie^a, Ruiyang Chen^a, Kazuhiro Yanagi^c, Weilu Gao^a,*

^a Department of Electrical and Computer Engineering, The University of Utah, 50 S Central Campus Drive, Salt Lake City, 84112, UT, USA

^b Department of Applied Physics, Stanford University, 348 Via Pueblo, Stanford, 94305, CA, USA

^c Department of Physics, Tokyo Metropolitan University, 1-1 Minami-Osawa, Hachioji-shi, Tokyo, 192-0397, Japan

ARTICLE INFO

Keywords:

Single-enantiomer carbon nanotube
Transfer matrix
GPU acceleration
Backpropagation algorithm
Phase change material
Reconfigurable chiral photonic devices

ABSTRACT

The interaction of circularly polarized light with chiral matter and functional devices enables novel phenomena and applications. Recently, macroscopic solid-state single-enantiomer carbon nanotube (CNT) films have become feasible and are emerging as a chiral photonic material platform thanks to their quantum-confinement-induced optical properties and facile scalable assembly. However, optical modeling, solver, and device design tools for such materials are non-existent. Here, we prepare macroscopic single-enantiomer (6,5) and (11,-5) randomly oriented CNT films and create an optical material model based on measured experimental optical spectra. We also implement a highly-parallel graphic-processing-unit accelerated transfer matrix solver for general bi-anisotropic materials and layered structures. Further, we demonstrate reconfigurable chiral photonic devices in a heterostructure with phase change materials through machine learning-enabled efficient gradient-based inverse design and optimization. Our developed full stack of a chiral photonic material and device hardware platform and a corresponding high-performance differential-programming-enabled solver opens the door for future chiral photonic devices and applications based on single-enantiomer CNT films.

1. Introduction

Manipulating the interaction of circularly polarized light with chiral materials and their functional photonic devices is crucial for many applications, such as sensing [1,2], imaging [3,4], computing [5], and quantum technologies [6]. The advancement of developing such devices is nowadays hindered not only by the limited number of high-performance material platforms but also by efficient solvers and design tools. In current material platforms, small natural chiral molecules generally have weak chiroptical responses because of a large mismatch between molecule size and optical wavelength. Chiral organic supramolecular structures [7,8] and twisted structures of anisotropic materials [9] manufactured through cost-effective bottom-up self-assembly techniques can produce strong chiroptical responses, while individual constituents lack quantum-confinement-induced extraordinary properties and the design of structures is largely empirical. Artificial symmetry-breaking periodic structures can provide an engineerable platform with systematic electromagnetic design tools, such as finite difference time domain analysis, while their top-down manufacturing is sophisticated and challenging to scale up [10] and those design tools are generally computationally intensive and time-consuming [11].

Carbon nanotubes (CNTs) resurge as a promising chiral photonic material platform in the form of both natural and synthetic chirality thanks to the recent progress in large-scale chirality and enantiomer separation and bottom-up macroscopic ordered self-assembly techniques [12–21]. The optical properties of CNTs are determined by their one-dimensional (1D) atomic structures [22]. The quantum confinement in 1D nanoscale tubular geometry of CNTs leads to the formation of subbands and the interband transitions between subbands produce strong exciton-dominant optical spectral features. The transition energies can be tuned by the quantum engineering of CNT atomic structures, which are typically described by a pair of chirality indices (n , m), and by external stimuli such as electric fields and optical excitation. Except for special highly symmetric zigzag (n ,0) and armchair (n , n) CNTs, all other CNTs are chiral and contain two enantiomers, denoted as (n , m) and ($n + m$, $-m$), with different chiral photonic responses. For example, as illustrated in Fig. 1, the interaction of (6,5) and (11,-5) CNTs of opposite handednesses with left circularly polarized (LCP) and right circularly polarized (RCP) light, such as circular dichroism (CD) that is the differential absorption of LCP and

* Corresponding author.

E-mail address: weilu.gao@utah.edu (W. Gao).

<https://doi.org/10.1016/j.carbon.2025.120016>

Received 11 October 2024; Received in revised form 7 January 2025; Accepted 13 January 2025

Available online 22 January 2025

0008-6223/© 2025 Elsevier Ltd. All rights are reserved, including those for text and data mining, AI training, and similar technologies.

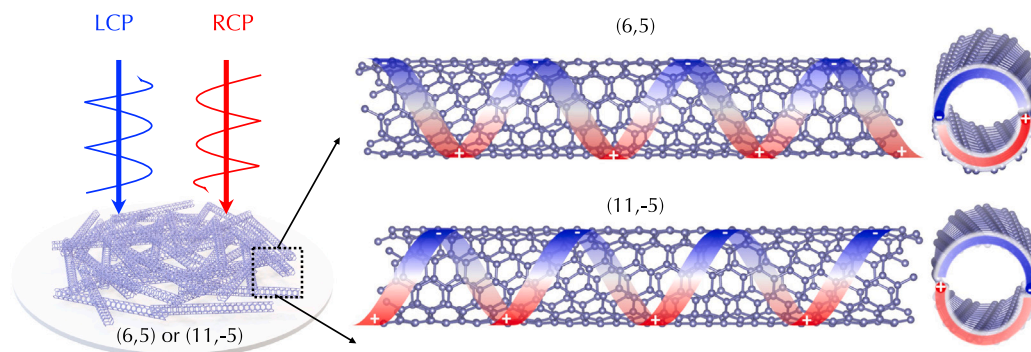


Fig. 1. Overview. Illustrations of the interaction of circularly polarized light with single-enantiomer CNT films and their excitonic chiral photonic responses. Schematics of CNTs were produced using VESTA [23].

RCP light, is distinctly different. Hence, their assembled macroscopic films become a solid-state material platform for building novel chiral photonic devices; see Fig. 1. However, to date, there is no demonstration of any optical modeling or solvers for such materials, hindering device design capability.

Here, we present an optical material model and a highly-parallel fast solver for macroscopic single-enantiomer (6,5) and (11,-5) randomly oriented CNT films, and demonstrate reconfigurable chiral photonic devices in a heterostructure with phase change materials (PCMs) through machine learning (ML)-enabled efficient gradient-based inverse design and optimization. Specifically, we prepared single-enantiomer (6,5) and (11,-5) suspensions through gel chromatography and macroscopic randomly oriented films through vacuum filtration, and experimentally measured CD and absorption spectra of suspension and solid-state samples. We created material models for (6,5) and (11,-5) films and implemented a graphic-processing-unit (GPU) accelerated transfer matrix solver for general bi-anisotropic materials and layered architectures based on a state-of-the-art ML framework. By simultaneously fitting experimental spectra, we extracted dielectric functions and chirality parameters for (6,5) and (11,-5) films. Furthermore, we leveraged the backpropagation algorithm in the ML framework to design a novel reconfigurable chiral photonic device based on a heterostructure consisting of single-enantiomer CNT films and PCM films. Our developed full stack of a chiral photonic material and device hardware platform and a corresponding GPU-accelerated and differential-programming-enabled solver opens the door for future chiral photonic devices and applications based on single-enantiomer CNT films.

2. Experimental section

2.1. Preparation of single-enantiomer CNT suspensions

We purchased CoMoCAT CNT powders and mixed them with a combination of surfactants. The mixture was tip-sonicated to disperse CNTs to form a homogenized aqueous suspension. The suspension was then purified through ultracentrifugation to remove undispersed impurities, such as catalysts and large bundles. The supernatant was collected for enantiomer separation, which was performed through an automatic temperature-controlled chromatography system for large-scale separation following the procedures described in Ref. [14,15,24]. By controlling the composition and concentration of surfactant elution solutions, CNTs of different diameters and handednesses were collected at various times during the process; see more details in Supporting Information Note 1. Fig. 2a displays a photograph of a prepared single-enantiomer suspension. During the separation process, we characterized the quality of suspensions by measuring their absorption spectra using an ultraviolet-visible-near infrared (UV-Vis-NIR) spectrometer (Shimadzu UV-3600 UV-Vis-NIR Spectrophotometer) in a wavelength range from 200 to 1200 nm. Fig. S1 displays a normalized

absorption spectrum of a separated (11,-5) suspension (red line). The spectrum was normalized with respect to the E_{11} peak. By repeating the enantiomer separation process multiple times, we collected enough CNT suspensions for preparing macroscopic films.

2.2. Preparation of single-enantiomer CNT films

We produced macroscopic (e.g., $5 \times 5 \text{ mm}^2$) single-enantiomer (6,5) and (11,-5) CNT films using vacuum filtration. Briefly, we exchanged the mixed surfactant system in separated single-enantiomer suspensions to a single sodium deoxycholate (DOC) surfactant system before pouring it into the filtration system. The DOC concentration was kept higher than its critical micelle concentration and a fast filtration was performed to produce randomly oriented films instead of highly aligned ones [18]. When all suspensions finished filtration, the deposited films were kept on the filtration system for a complete dry. The obtained films on the filter membrane can be transferred onto arbitrary substrates following a wet transfer process [18]; see more details in Supporting Information Note 2. For optical characterization, we transferred films onto silica substrates, which have broadband optical transparency from ultraviolet to near-infrared wavelength ranges. Fig. 2b shows a photo of a produced film. Due to the self-limiting nature of the vacuum filtration process [25,26], the film thickness was uniform and can be controlled by adjusting the suspension concentration and volume. The film lateral size will be potentially scalable to be wafer-scale using large-scale filtration systems.

2.3. Film thickness measurement and morphological characterization

We measured the thicknesses of obtained films through atomic force microscopy (Bruker Multimode 8 AFM). Fig. S2a displays a representative AFM image of one CNT film. The film thickness was measured by creating a section profile that crossed a crack in the film, leading to a relatively smooth edge. In contrast, multiple bumps formed around the physical edge of the film because the film was cut into certain shapes manually. Fig. S2b shows the height profile of the film with a thickness of $\sim 60 \text{ nm}$. Further, we characterized the surface morphology of obtained films using scanning electron microscopy (FEI Teneo SEM). Fig. S3 shows SEM images of one prepared single-enantiomer CNT film at two different positions. Some areas showed randomly oriented structures (Position 1) while other areas displayed the formation of local, microscopic, oriented structures (Position 2).

2.4. Characterization of optical linear anisotropy

We verified the optical linear anisotropy of obtained films by measuring linear-polarization-dependent optical attenuation. We used a laser at a wavelength of 635 nm (Thorlabs, CPS635R) incident on obtained films. The circular beam size was $\sim 2 \text{ mm}$ in diameter to probe

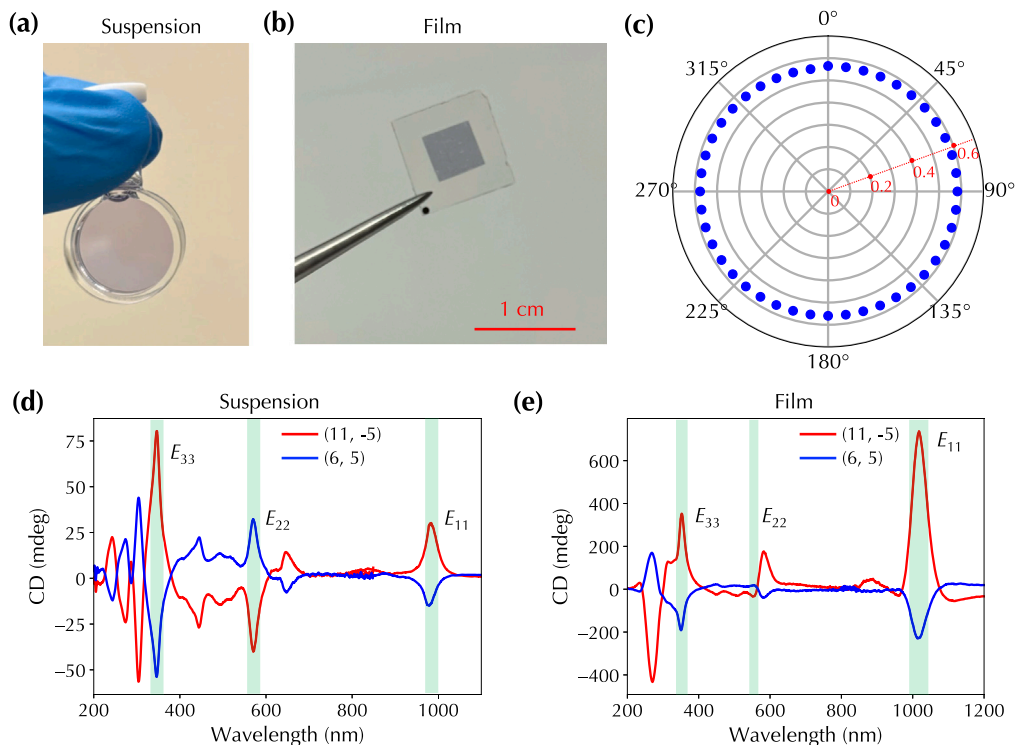


Fig. 2. Experimental results. Photos of (a) separated single-enantiomer suspensions and (b) macroscopic films. (c) Polar plot of polarization-dependent transmission of one obtained film. CD spectra of single-enantiomer (6,5) and (11,-5) (d) suspensions and (e) macroscopic films. (For interpretation of the references to color in this figure legend, the reader is referred to the web version of this article.)

the degree of alignment in a large area. The linear polarization state of the laser was rotated through a half-waveplate (Thorlabs, WPH10ME-633). The transmitted optical power was measured by a photodiode (Thorlabs, PM16-130). The transmitted optical power of both CNT samples and a bare reference substrate was measured and the ratio was calculated as transmittance. Fig. 2c shows a polar plot of measured transmittance at various polarization angles and there was no clear angle dependence, confirming that obtained films were macroscopically randomly oriented.

2.5. CD spectra measurement and enantiomeric purity

We measured the CD and absorption spectra of separated single-enantiomer suspensions and macroscopic films using a Jasco CD J-1500 spectrometer under normal incidence. The circular probe beam size was ~ 2 mm in diameter. The absorption spectra measured from the CD spectrometer are expressed as $(A_L + A_R)/2$, where A_L and A_R are the absorption spectra when the incident light is LCP and RCP, respectively. These spectra are equivalent to the absorption spectra measured from commercial UV-Vis-NIR spectrometers because the incident light in UV-Vis-NIR spectrometers is unpolarized and can be treated as a combination of equal amount of LCP and RCP light. Fig. S1 shows two normalized absorption spectra of two similarly separated (11,-5) suspensions measured using UV-Vis-NIR and CD spectrometers, respectively. Both spectra were normalized with respect to their E_{11} peaks and were nearly identical. The g factor was calculated as the ratio between CD and average absorption, which was measured from the CD spectrometer and expressed as $(A_L + A_R)/2$. Fig. 2d shows the measured CD spectra of single-enantiomer (6,5) and (11,-5) suspensions in a wavelength range from 200 to 1200 nm. The excitonic interband transitions with the same band indices for valance and conduction bands, such as E_{11} , E_{22} , and E_{33} , correspond to the CD spectral features in green shaded rectangles of Fig. 2d with alternating signs [13–15,27].

Other peaks are mainly from cross-polarized excitons [14]. Fig. S4a and S4b show the corresponding absorption and g factor spectra. Based on the ratio of CD and absorption peaks at the E_{22} location, denoted as CD_{norm} , we estimated enantiomeric purities (EPs) for (6,5) and (11,-5) suspensions following two linear regression fitting curves, $EP(6,5) (\%) = 50 + \alpha CD_{\text{norm}}$ and $EP(11,-5) (\%) = 50 - \alpha CD_{\text{norm}}$, where $\alpha = 0.421 \text{ mdeg}^{-1}$ [14]. Hence, the calculated EPs for (6,5) and (11,-5) suspensions were nearly the same $\sim 87\%$.

Further, we measured the CD and absorption spectra of macroscopic single-enantiomer (6,5) and (11,-5) randomly oriented films. In contrast to suspension measurements, the CD measurements of solid-state samples require special treatment to eliminate instrumentation artifacts. We adopted a “four-configuration” approach, where CD spectra were captured under four different sample configurations as shown in Fig. S5a, and thus the averaged CD spectra removed artifacts and provided the genuine CD response from samples [20]; see *Supporting Information Note 3*, Fig. S5b, and Fig. S5c for more details. Fig. 2e, Fig. S6a, Fig. S6b display the measured CD, absorption, and g factor spectra of single-enantiomer (6,5) and (11,-5) random films in a wavelength range from 200 to 1200 nm, respectively. The assignment of excitonic transitions in the film CD spectra (green shaded rectangles in Fig. 2e) also followed the rule of alternating signs. Compared to suspension CD and absorption spectra, as expected, the excitonic peaks in films become broadened due to CNT bundling. Interestingly, the relative heights of E_{11} , E_{22} , and E_{33} peaks in films are substantially different from those in suspensions, and E_{11} becomes the strongest in films. Moreover, the peak heights of the same excitonic transitions for two enantiomers are asymmetric, even though the thicknesses of two enantiomer films are nearly the same as evidenced in absorption spectra shown in Fig. S6a and the purities of suspensions are almost identical. Moreover, the degree of the peak height asymmetry is different for different excitonic transitions. For example, the E_{11} transition shows a three-time difference while the E_{33} transition shows a two-time

difference.

We attributed these distinctions in CD spectra between suspensions and films to the formation of local, microscopic twisted stack architecture; see the illustration in Fig. S7. Although obtained films were nearly isotropic in a mm²-size area characterized using the optical approach, local orientations could form on a microscopic scale (nm² to μm² size) as evidenced in scanning electron microscopy images shown in Fig. S3, and could form anywhere in the film thickness direction during the vacuum filtration process. Orientation directions could be randomly selected across the thickness, possibly forming the twisted stack architecture. The structure-induced chirality in this architecture can also produce CD responses because of the helical arrangement of 1D CNT excitonic dipoles [20] and the signs of CD response depend on the twist direction. Hence, the observed CD responses of single-enantiomer CNT films have combined contributions from the intrinsic chirality of enantiomers and the structure-induced chirality of microscopic twisted stacks, leading to asymmetric peak heights of the same excitonic transitions in (6,5) and (11,−5) films. If the twisted direction is the same as one enantiomer handedness, these two contributions enhance each other to have a boosted CD signal. In contrast, the twist direction of the same twisted stack is opposite to the handedness of the other enantiomer, these two contributions counteract to have a reduced CD signal. Furthermore, the CD contribution from the twisted stack is mainly dependent on the dielectric function while the CD contribution from enantiomers is mainly from the chirality parameter, as described below. Hence, for the same twisted stack and enantiomer, if the relative strength between the chirality parameter and dielectric function is different, the degree of asymmetry can also be different. Since the film absorption is related to the dielectric function, the g factor can be a good indicator of the relative strength between these two quantities. For example, the g factor in the E_{33} region is larger than that in the E_{11} region, suggesting a larger contribution from the enantiomer intrinsic chirality and a smaller contribution from the twisted stack structure-induced chirality in the E_{33} region than those in the E_{11} region. Hence, the degree of asymmetry of peak heights in the E_{33} region appears less than that in the E_{11} region. It is challenging to eliminate the formation of twist structures during film preparation, but we can combine the contributions of CD signals from chiral atomic structures and twisted stacks and treat them as a phenomenological and effective material parameter for designing optoelectronic devices.

3. Results and discussion

3.1. Transfer matrix and fitting material parameters

On the macroscopic level, randomly oriented single-enantiomer CNT films can be treated as a reciprocal, chiral, bi-anisotropic medium with constitutive relations written as $\vec{D} = \vec{\epsilon}\vec{E} + \vec{\xi}\vec{H}$ and $\vec{B} = \vec{\zeta}\vec{E} + \vec{\mu}\vec{H}$, where \vec{D} is displacement field, \vec{E} is electric field, \vec{H} is magnetic field, \vec{B} is magnetic flux density, ϵ is electric permittivity or dielectric function tensor, μ is magnetic permeability tensor, and $\vec{\xi}$ and $\vec{\zeta}$ are two magnetoelectric tensors describing the coupling between electric and magnetic components in constitutive relations [28]. Further, $\vec{\xi}$ and $\vec{\zeta}$ can be expressed as $\sqrt{\epsilon_0\mu_0}(\vec{\chi} - j\vec{\kappa})$ and $\sqrt{\epsilon_0\mu_0}(\vec{\chi} + j\vec{\kappa})$, respectively, where $\vec{\chi}$ and $\vec{\kappa}$ are two unitless magnetoelectric tensors. Since our produced single-enantiomer CNT films are reciprocal and chiral, $\vec{\chi}$ is thus diminishing and $\vec{\kappa}$ is specifically called the chirality parameter.

In this work, we focused on the E_{11} transitions in (6,5) and (11,−5) films because their CD responses are distant from cross-polarized transitions and have little spectral interference from these transitions. We expressed the relative electric permittivity tensor for a CNT film, $\vec{\epsilon}_{\text{CNT}}$, as

$$\vec{\epsilon}_{\text{CNT}} = \begin{bmatrix} \epsilon_{\text{in}} & 0 & 0 \\ 0 & \epsilon_{\text{in}} & 0 \\ 0 & 0 & \epsilon_{\text{out}} \end{bmatrix},$$

where ϵ_{in} and ϵ_{out} are in-plane and out-of-plane dielectric functions. ϵ_{in} is a function of angular frequency ω and described using a Lorentz oscillator model as

$$\epsilon_{\text{in}}(\omega) = \epsilon_{\infty} + \frac{\omega_p^2}{\omega_0^2 - \omega^2 - j\omega\Gamma},$$

where ϵ_{∞} is a constant, ω_p is plasma frequency, ω_0 is the resonance frequency for E_{11} transition, and Γ is the corresponding decay rate. ϵ_{out} is a constant as ~ 3.4 determined in Ref. [29] since cross-polarization transitions are negligible around the E_{11} transition. In addition, since materials are non-magnetic, $\vec{\mu}$ was assumed to be a scalar constant μ_0 , which is the vacuum magnetic permeability.

Moreover, we assumed $\vec{\kappa}$ tensor as an isotropic scalar function $\kappa(\omega)$. We would like to note that the CD contribution from chiral atomic arrangements in (6,5) and (11,−5) enantiomers should be isotropic while the CD contribution from twisted stacks could possibly be anisotropic between in-plane and out-of-plane components. However, under our current capacity with only normal incidence CD experiments, a close examination of the out-of-plane chirality parameter is not feasible. A carefully crafted custom CD spectrometer with the removal of artifacts and extrinsic effects in solid-state samples will be needed, which is beyond the scope of our current work.

We described $\kappa(\omega)$ using a Condon model [30]. Since E_{11} transitions lie far away from other transitions, the Condon model has one dominant resonance and $\kappa(\omega)$ becomes

$$\kappa(\omega) = \frac{\omega R}{\omega_1^2 - \omega^2 + j\omega\Gamma_1},$$

where R is the rotational strength of transitions, ω_1 is the resonance frequency for E_{11} transition, and Γ_1 is the corresponding decay rate. Note that ω_1 is close to but not necessarily identical to ω_0 in dielectric function expression because there is an observable slight difference of the peaks in experimental CD and absorption spectra as shown before.

We then developed a transfer matrix solver for general bi-anisotropic materials and their layered architectures [31] to fit CD and absorption spectra to extract $\epsilon_{\text{in}}(\omega)$ and $\kappa(\omega)$ as illustrated in the inset panel of Fig. 3a and Fig. S8. In the medium of the incident light, the electric field vector $\vec{E}(\vec{r})$ and magnetic field vector $\vec{H}(\vec{r})$ propagating along z axis can be expressed as

$$\vec{E}(\vec{r}) = \vec{e}(z)e^{jq(x\cos\psi + y\sin\psi)},$$

$$\vec{H}(\vec{r}) = \vec{h}(z)e^{jq(x\cos\psi + y\sin\psi)},$$

where $q = k_0 n_1 \sin\theta_i$ is complex-valued wavenumber, ψ is azimuthal angle, θ_i is incident angle, n_1 is refractive index of incident light medium, $\vec{e}(z)$ is the unit vector as $e_x(z)\hat{x} + e_y(z)\hat{y} + e_z(z)\hat{z}$, and $\vec{h}(z)$ is the unit vector as $h_x(z)\hat{x} + h_y(z)\hat{y} + h_z(z)\hat{z}$. For z -components, we have $e_z(z) = v_{zx}^{ee}e_x(z) + v_{zy}^{ee}e_y(z) + v_{zx}^{eh}h_x(z) + v_{zy}^{eh}h_y(z)$ and $h_z(z) = v_{zx}^{he}e_x(z) + v_{zy}^{he}e_y(z) + v_{zx}^{hh}h_x(z) + v_{zy}^{hh}h_y(z)$ because of the coupled electric and magnetic fields in constitutive relations.

By solving the Maxwell's equations and matching boundary conditions, we have

$$v_{zx}^{ee} = -\frac{\mu_{zz}\epsilon_{zx} - \epsilon_{zz}[\zeta_{zx} + (q/\omega)\sin\psi]}{\epsilon_{zz}\mu_{zz} - \epsilon_{zz}\zeta_{zz}}, v_{zy}^{ee} = -\frac{\mu_{zz}\epsilon_{zy} - \epsilon_{zz}[\zeta_{zy} - (q/\omega)\cos\psi]}{\epsilon_{zz}\mu_{zz} - \epsilon_{zz}\zeta_{zz}},$$

$$v_{zx}^{eh} = \frac{\epsilon_{zz}\mu_{zx} - \mu_{zz}[\xi_{zx} - (q/\omega)\sin\psi]}{\epsilon_{zz}\mu_{zz} - \epsilon_{zz}\zeta_{zz}}, v_{zy}^{eh} = \frac{\epsilon_{zz}\mu_{zy} - \mu_{zz}[\xi_{zy} + (q/\omega)\cos\psi]}{\epsilon_{zz}\mu_{zz} - \epsilon_{zz}\zeta_{zz}},$$

$$v_{zx}^{he} = \frac{\zeta_{zz}\epsilon_{zx} - \epsilon_{zz}[\zeta_{zx} + (q/\omega)\sin\psi]}{\epsilon_{zz}\mu_{zz} - \epsilon_{zz}\zeta_{zz}}, v_{zy}^{he} = \frac{\zeta_{zz}\epsilon_{zy} - \epsilon_{zz}[\zeta_{zy} - (q/\omega)\cos\psi]}{\epsilon_{zz}\mu_{zz} - \epsilon_{zz}\zeta_{zz}},$$

$$v_{zx}^{hh} = -\frac{\epsilon_{zz}\mu_{zx} - \zeta_{zz}[\xi_{zx} - (q/\omega)\sin\psi]}{\epsilon_{zz}\mu_{zz} - \epsilon_{zz}\zeta_{zz}}, v_{zy}^{hh} = -\frac{\epsilon_{zz}\mu_{zy} - \zeta_{zz}[\xi_{zy} + (q/\omega)\cos\psi]}{\epsilon_{zz}\mu_{zz} - \epsilon_{zz}\zeta_{zz}},$$

where ϵ_{ij} , μ_{ij} , ξ_{ij} , ζ_{ij} , $i, j \in \{x, y, z\}$ are tensor components of $\vec{\epsilon}$, $\vec{\mu}$, $\vec{\xi}$, and $\vec{\zeta}$, respectively, for materials in each layer. Furthermore, there are \mathbf{P}_m and \mathbf{M}_m matrices for m th layer with a thickness d_m , which are expressed as

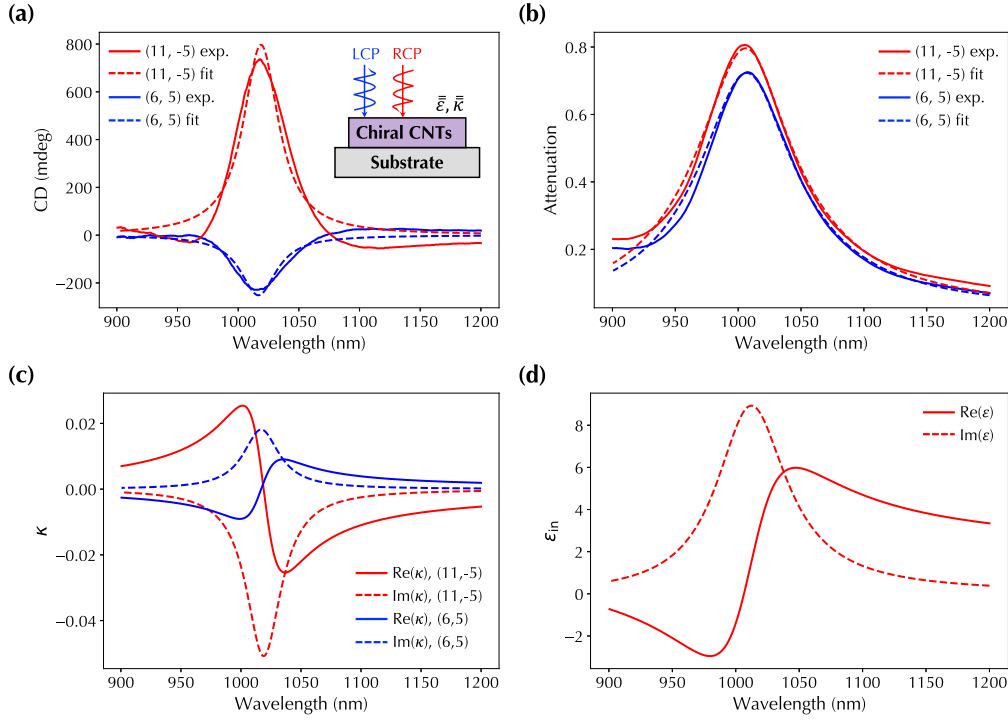


Fig. 3. Transfer matrix fitting. Experimental and fitting (a) CD spectra and (b) absorption spectra of (6,5) and (11,−5) single-enantiomer films. Extracted complex-valued (c) chirality parameters and (d) dielectric functions.

$$\mathbf{P}_m = \omega \begin{bmatrix} \zeta_{yx} & \zeta_{yy} & \mu_{yx} & \mu_{yy} \\ -\zeta_{xx} & -\zeta_{xy} & -\mu_{xx} & -\mu_{xy} \\ -\epsilon_{yx} & -\epsilon_{yy} & -\xi_{yx} & -\xi_{yy} \\ \epsilon_{xx} & \epsilon_{xy} & \xi_{xx} & \xi_{xy} \end{bmatrix} + \begin{bmatrix} \zeta_{yz} + \frac{a}{\omega} \cos\psi & 0 & 0 & 0 \\ 0 & -\zeta_{xz} + \frac{a}{\omega} \sin\psi & 0 & 0 \\ 0 & 0 & -\epsilon_{yz} & 0 \\ 0 & 0 & 0 & \epsilon_{xz} \end{bmatrix} \cdot \mathbf{J} \cdot \begin{bmatrix} v_{zx}^{ee} & 0 & 0 & 0 \\ 0 & v_{zy}^{ee} & 0 & 0 \\ 0 & 0 & v_{zx}^{eh} & 0 \\ 0 & 0 & 0 & v_{zy}^{eh} \end{bmatrix} + \begin{bmatrix} \mu_{yz} & 0 & 0 & 0 \\ 0 & -\mu_{xz} & 0 & 0 \\ 0 & 0 & -\xi_{yz} + \frac{a}{\omega} \cos\psi & 0 \\ 0 & 0 & 0 & \xi_{xz} + \frac{a}{\omega} \sin\psi \end{bmatrix} \cdot \mathbf{J} \cdot \begin{bmatrix} v_{zx}^{he} & 0 & 0 & 0 \\ 0 & v_{zy}^{he} & 0 & 0 \\ 0 & 0 & v_{zx}^{hh} & 0 \\ 0 & 0 & 0 & v_{zy}^{hh} \end{bmatrix}$$

with

$$\mathbf{J} = \begin{bmatrix} 1 & 1 & 1 & 1 \\ 1 & 1 & 1 & 1 \\ 1 & 1 & 1 & 1 \\ 1 & 1 & 1 & 1 \end{bmatrix}$$

and

$$\mathbf{M}_m = e^{i\mathbf{P}_m d_m}.$$

There are \mathbf{K}_{inc} and \mathbf{K}_{tr} matrices for the incident and transmission layers with the incident angle θ_i and output angle θ_{tr} , which are expressed as

$$\mathbf{K}_{\text{inc}} = \begin{bmatrix} -\sin\psi & -\cos\psi \cos\theta_i & -\sin\psi & \cos\psi \cos\theta_i \\ \cos\psi & -\sin\psi \cos\theta_i & \cos\psi & \sin\psi \cos\theta_i \\ -\left(\frac{n_1}{\eta_0}\right) \cos\psi \cos\theta_i & \left(\frac{n_1}{\eta_0}\right) \sin\psi & \left(\frac{n_1}{\eta_0}\right) \cos\psi \cos\theta_i & \left(\frac{n_1}{\eta_0}\right) \sin\psi \\ -\left(\frac{n_1}{\eta_0}\right) \sin\psi \cos\theta_i & -\left(\frac{n_1}{\eta_0}\right) \cos\psi & \left(\frac{n_1}{\eta_0}\right) \sin\psi \cos\theta_i & -\left(\frac{n_1}{\eta_0}\right) \cos\psi \end{bmatrix}$$

and

$$\mathbf{K}_{\text{tr}} = \begin{bmatrix} -\sin\psi & -\cos\psi \cos\theta_{\text{tr}} & -\sin\psi & \cos\psi \cos\theta_{\text{tr}} \\ \cos\psi & -\sin\psi \cos\theta_{\text{tr}} & \cos\psi & \sin\psi \cos\theta_{\text{tr}} \\ -\left(\frac{n_2}{\eta_0}\right) \cos\psi \cos\theta_{\text{tr}} & \left(\frac{n_2}{\eta_0}\right) \sin\psi & \left(\frac{n_2}{\eta_0}\right) \cos\psi \cos\theta_{\text{tr}} & \left(\frac{n_2}{\eta_0}\right) \sin\psi \\ -\left(\frac{n_2}{\eta_0}\right) \sin\psi \cos\theta_{\text{tr}} & -\left(\frac{n_2}{\eta_0}\right) \cos\psi & \left(\frac{n_2}{\eta_0}\right) \sin\psi \cos\theta_{\text{tr}} & -\left(\frac{n_2}{\eta_0}\right) \cos\psi \end{bmatrix}.$$

Hence, the overall transfer matrix $\mathbf{Q} = \mathbf{K}_{\text{tr}}^{-1} \left(\prod_{m=1}^N \mathbf{M}_m \right) \mathbf{K}_{\text{inc}}$, where N is the total number of layers. The input and output vectors are related as

$$\begin{bmatrix} t_s \\ t_p \\ 0 \\ 0 \end{bmatrix} = \mathbf{Q} \cdot \begin{bmatrix} a_s \\ a_p \\ r_s \\ r_p \end{bmatrix} = \begin{bmatrix} Q_{00} & Q_{01} & Q_{02} & Q_{03} \\ Q_{10} & Q_{11} & Q_{12} & Q_{13} \\ Q_{20} & Q_{21} & Q_{22} & Q_{23} \\ Q_{30} & Q_{31} & Q_{32} & Q_{33} \end{bmatrix} \cdot \begin{bmatrix} a_s \\ a_p \\ r_s \\ r_p \end{bmatrix}.$$

Since we have

$$\begin{bmatrix} r_s \\ r_p \end{bmatrix} = \begin{bmatrix} r_{ss} & r_{sp} \\ r_{ps} & r_{pp} \end{bmatrix} \cdot \begin{bmatrix} a_s \\ a_p \end{bmatrix},$$

and

$$\begin{bmatrix} t_s \\ t_p \end{bmatrix} = \begin{bmatrix} t_{ss} & t_{sp} \\ t_{ps} & t_{pp} \end{bmatrix} \cdot \begin{bmatrix} a_s \\ a_p \end{bmatrix},$$

we can represent all reflection and transmission coefficients under different combinations of polarization states based on elements of matrix \mathbf{Q} . Specifically, we have reflection and transmission coefficients under linear polarizations as

$$\begin{aligned} r_{ss} &= \frac{Q_{30}Q_{23} - Q_{33}Q_{20}}{Q_{22}Q_{23} - Q_{23}Q_{32}}, & r_{sp} &= \frac{Q_{31}Q_{23} - Q_{33}Q_{21}}{Q_{22}Q_{23} - Q_{23}Q_{32}}, \\ r_{ps} &= \frac{Q_{32}Q_{20} - Q_{30}Q_{22}}{Q_{22}Q_{23} - Q_{23}Q_{32}}, & r_{pp} &= \frac{Q_{32}Q_{21} - Q_{31}Q_{22}}{Q_{22}Q_{23} - Q_{23}Q_{32}}, \\ t_{ss} &= Q_{00} + Q_{02}r_{ss} + Q_{03}r_{ps}, & t_{sp} &= Q_{01} + Q_{02}r_{sp} + Q_{03}r_{pp}, \\ t_{ps} &= Q_{10} + Q_{12}r_{ss} + Q_{13}r_{ps}, & t_{pp} &= Q_{11} + Q_{12}r_{sp} + Q_{13}r_{pp}. \end{aligned}$$

and coefficients under circular polarizations as

$$\begin{aligned} r_{LL} &= -\frac{r_{ss} + r_{pp} + j(r_{sp} - r_{ps})}{2}, & r_{LR} &= \frac{r_{ss} - r_{pp} - j(r_{sp} + r_{ps})}{2}, \\ r_{RL} &= \frac{r_{ss} - r_{pp} + j(r_{sp} + r_{ps})}{2}, & r_{RR} &= -\frac{r_{ss} + r_{pp} - j(r_{sp} - r_{ps})}{2}, \\ t_{LL} &= \frac{t_{ss} + t_{pp} + j(t_{sp} - t_{ps})}{2}, & t_{LR} &= -\frac{t_{ss} - t_{pp} - j(t_{sp} + t_{ps})}{2}, \\ t_{RL} &= -\frac{t_{ss} - t_{pp} + j(t_{sp} + t_{ps})}{2}, & t_{RR} &= \frac{t_{ss} + t_{pp} - j(t_{sp} - t_{ps})}{2}. \end{aligned}$$

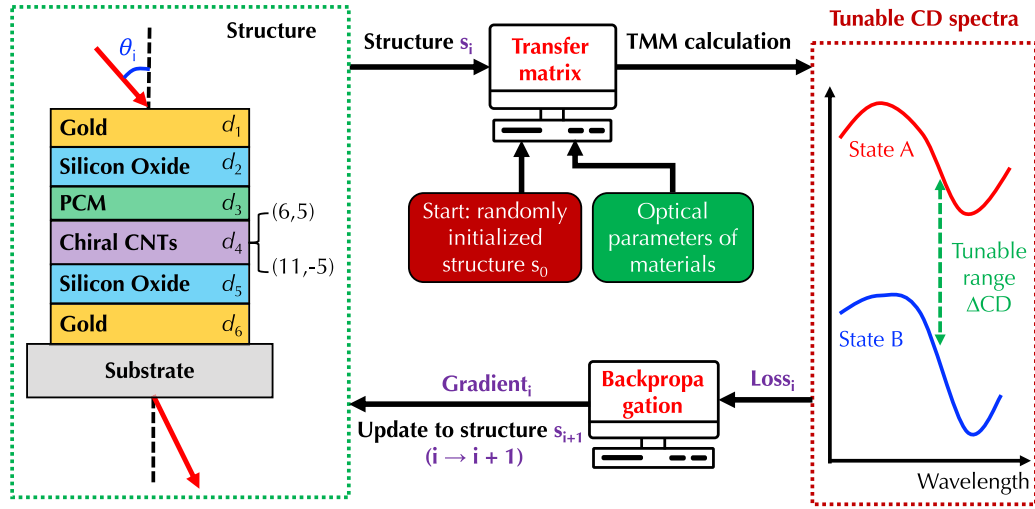


Fig. 4. Optimization flowchart. Illustration of employing GPU-accelerated calculations and backpropagation-enabled optimizations for designing reconfigurable chiral photonic devices.

Hence, we can obtain circular reflectance and transmittance for any polarization combination with $R = |r|^2$ and $T = \frac{n_2 \text{Re}(\cos\theta_{tr})}{n_1 \cos\theta_{tr}} |t|^2$. Attenuation is defined as $A = -\log_{10} T$, CD is defined as $A_L - A_R$, and average absorption is $(A_L + A_R)/2$. Here, $A_L = -\log_{10}(T_{LL} + T_{RL})$ is the attenuation for a LCP incident light and $A_R = -\log_{10}(T_{RR} + T_{LR})$ is the attenuation for a RCP incident light.

We employed the developed transfer matrix to simultaneously fit the CD and absorption spectra of obtained single-enantiomer (6,5) and (11,−5) films and extract material parameters, including $\omega_\infty, \omega_p, \omega_0, \omega_1, \Gamma, \Gamma_1$, and R in ϵ_{in} and κ . We assumed that ϵ_{in} was the same for (6,5) and (11,−5) CNTs while κ was different. Figs. 3a and 3b display the experimental and fitting CD and absorption spectra for both films, showing a good agreement. Figs. 3c and 3d display the extracted complex-valued κ and ϵ_{in} . Note that κ of the (11,−5) film is larger than that of the (6,5) film because the CD signals of the (11,−5) film is larger and κ was treated as an effective parameter to include contributions from both intrinsic and structure-induced chiralities. The developed transfer matrix solver and material models were uploaded to a public open-source repository.¹

3.2. ML-accelerated calculation and design of reconfigurable chiral photonic devices

Since all mathematical operations in transfer matrix calculations are based on tensor algebra, we leveraged the state-of-the-art ML framework, PyTorch, to implement the transfer matrix solver so that the calculations can be substantially accelerated on GPU hardware. Further, we were able to employ the gradient-based backpropagation algorithm in PyTorch to design chiral photonic devices. Fig. 4 illustrates the flowchart of designing a heterostack architecture consisting of single-enantiomer (6,5) or (11,−5) CNT randomly oriented films and phase change material (PCM) films for reconfigurable chiral photonic devices [21]. Upon the excitation of electrical or optical pulses, PCMs can be fast and reversely reconfigured between crystalline and amorphous phases, leading to a substantial change of dielectric functions [32–35]. Furthermore, after the reconfigurability of PCMs, the optical properties of PCMs are preserved even after removing the excitation stimulus. In addition, PCMs are scalable and compatible with other materials for constructing complex architectures [36]. Such strong non-volatile reconfigurability of scalable PCM films make

them ideal for reconfigurable photonic devices in both free space [37–40] and integrated circuits [41–45]. The top and bottom gold layers and sandwiched silicon oxide layers are intended to provide multiple reflections to enhance the chiral light-matter interaction. From a practical perspective, silicon oxide layers can also protect PCMs from being exposed to the surrounding environment for a long device lifespan. We chose germanium-antimony-tellurium (GST) PCM for the demonstration because of its mature manufacturing and broad applications.

Our design target is to find the best combination of layer thicknesses $\{d_1, d_2, \dots, d_6\}$ under a given incidence angle θ_i to produce the largest tunable range of CD, denoted as ΔCD . The design started with a randomly initialized structure s_0 and known optical constants of materials. Specifically, we utilized the fitted material parameters of single-enantiomer (6,5) and (11,−5) CNT randomly oriented films and dielectric functions of GST, silicon oxide, and gold films from our prior work. [21,46] and public database² We performed the forward calculation of CD spectra under crystalline and amorphous GST phases and defined $-\Delta CD$ as the loss function. Hence, the minimization of the loss in the backpropagation algorithm is equivalent to maximizing ΔCD . Based on the calculated gradient, the structural parameters were updated to s_1 and these cycles were repeated multiple times to achieve optimal design.

Figs. 5a and 5b show 3D plots of optimal ΔCD after optimization under various θ_i and CNT thickness d_{CNT} for (11,−5) and (6,5) films, respectively. The values of optimal ΔCD in structures with (11,−5) films are larger than those in structures with (6,5) films because of the larger κ of (11,−5) films; see Fig. 3c. It is clear that large oblique incident angles and thick films produce strong reconfigurability because oblique incidence breaks mirror symmetry and generates strong CD response and thick films naturally have strong chiral light-matter interaction. Notably, there is no reconfigurability of CD response at normal incidence. It seems to contradict the intuition that multiple reflections between gold reflectors can enhance chiral light-matter interaction and changing the dielectric environment between reflectors can lead to CD change. It is noted that reflectors are still planar and symmetric and the incident circularly polarized light changes the handedness, such as from LCP to RCP light or from RCP to LCP light, upon the reflection. Hence, the handedness of circularly polarized light cannot be preserved during multiple reflections so there is no enhancement or reconfigurability.

¹ Open-source repository. https://github.com/GaoUtahLab/chiral_cnt_model.

² Refractive Index Database. <https://refractiveindex.info/>.

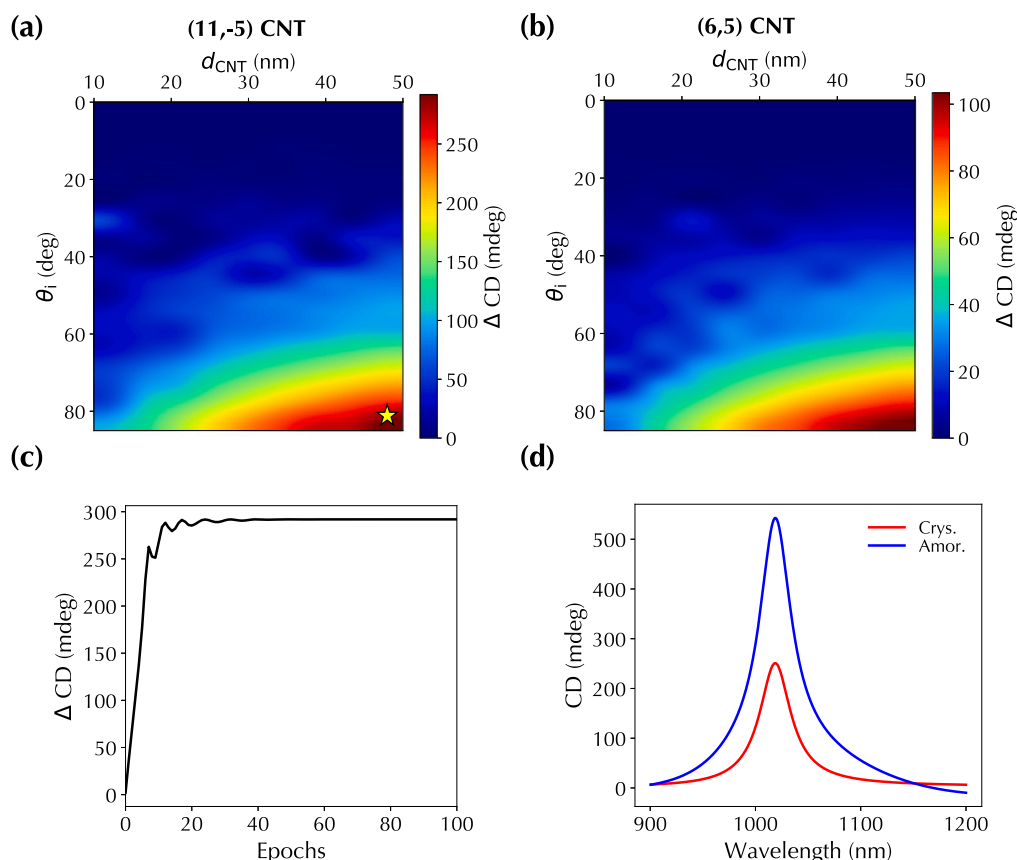


Fig. 5. Optimization results. 3D plots of optimal ΔCD after optimization under various θ_i and CNT thickness d_{CNT} for single-enantiomer (a) (11,-5) and (b) (6,5) films, respectively. (c) The optimization curve for the architecture showing the largest tunable at $\theta_i = 85^\circ$ and $d_{CNT} = 50$ nm. (d) CD spectra under crystalline and amorphous GST phases for a 50-nm thick (11,-5) film at $\theta_i = 85^\circ$ corresponding to the yellow star in (a).

Fig. 5c shows the evolution of ΔCD with iteration epochs, confirming a successful optimization driven by the backpropagation algorithm. Fig. 5d demonstrates the largest tunable range of CD spectra under crystalline and amorphous GST phases for a 50-nm thick (11,-5) film at $\theta_i = 85^\circ$ (yellow star in Fig. 5a), and Fig. S9a and S9b show the reconfigurability of corresponding absorption and g factor spectra, respectively. The tunable range gradually decreases with decreasing θ_i as shown in Fig. S10a–S10d.

4. Conclusions

In summary, we created an optical material model, developed a high-performance general transfer matrix solver, extracted material parameters, and efficiently designed and optimized a reconfigurable chiral photonic heterostructure with PCMs for macroscopic, randomly oriented, single-enantiomer (6,5) and (11,-5) CNT films. The demonstrated integrated hardware and software platform opens new opportunities for exploring both fundamental chiral phenomena and novel applications based on macroscopic solid-state CNT films.

CRediT authorship contribution statement

Jichao Fan: Writing – review & editing, Writing – original draft, Visualization, Validation, Methodology, Investigation, Formal analysis, Data curation. **Benjamin Hillam:** Writing – review & editing, Methodology, Investigation, Data curation. **Cheng Guo:** Writing – review & editing, Software, Methodology, Data curation. **Hiroyuki Fujinami:** Methodology, Data curation. **Koki Shiba:** Methodology, Data curation. **Haoyu Xie:** Methodology. **Ruiyang Chen:** Methodology. **Kazuhiro**

Yanagi: Writing – review & editing, Supervision, Methodology, Funding acquisition. **Weilu Gao:** Writing – review & editing, Writing – original draft, Visualization, Validation, Supervision, Software, Resources, Project administration, Methodology, Investigation, Funding acquisition, Formal analysis, Data curation, Conceptualization.

Declaration of competing interest

The authors declare that they have no known competing financial interests or personal relationships that could have appeared to influence the work reported in this paper.

Acknowledgments

J.F., B.H., H.X., R.C., and W.G. acknowledge the support from the National Science Foundation, United States through Grant Nos. 2230727, 2235276, 2316627, and 2321366. K.Y. acknowledges support from JSPS KAKENHI through Grant Nos. JP21H05017, JP23H00259, and JP24H01200, and U.S.-JAPAN PIRE through Grant No. JPJSJRP20221202, Japan, and ASPIRE project through Grant No. JPMJAP2310, Japan.

Appendix A. Supplementary data

Supplementary material related to this article can be found online at <https://doi.org/10.1016/j.carbon.2025.120016>.

References

- [1] Y. Liu, Z. Wu, D.W. Armstrong, H. Wolosker, Y. Zheng, Detection and analysis of chiral molecules as disease biomarkers, *Nat. Rev. Chem.* 7 (5) (2023) 355–373.

- [2] L.A. Warning, A.R. Mianashty, L.A. McCarthy, Q. Zhang, C.F. Landes, S. Link, Nanophotonic approaches for chirality sensing, *ACS Nano* 15 (10) (2021) 15538–15566.
- [3] X. Zhan, F.-F. Xu, Z. Zhou, Y. Yan, J. Yao, Y.S. Zhao, 3d laser displays based on circularly polarized lasing from cholesteric liquid crystal arrays, *Adv. Mater.* 33 (37) (2021) 2104418.
- [4] H.S. Khaliq, J. Kim, T. Naeem, K. Riaz, T. Badloe, J. Seong, J. Akbar, M. Zubair, M.Q. Mehmood, Y. Massoud, et al., Broadband chiro-optical effects for futuristic meta-holographic displays, *Adv. Opt. Mater.* 10 (22) (2022) 2201175.
- [5] S. Dan, S. Paramanik, A.J. Pal, Introducing chiro-optical activities in photonic synapses for neuromorphic computing and in-memory logic operations, *ACS Nano* (2024).
- [6] C.D. Aiello, J.M. Abendroth, M. Abbas, A. Afanasev, S. Agarwal, A.S. Banerjee, D.N. Beratan, J.N. Belling, B. Berche, A. Botana, et al., A chirality-based quantum leap, *ACS Nano* 16 (4) (2022) 4989–5035.
- [7] G. Albano, G. Pescitelli, L. Di Bari, Chiroptical properties in thin films of π -conjugated systems, *Chem. Rev.* 120 (18) (2020) 10145–10243.
- [8] F. Furlan, J.M. Moreno-Naranjo, N. Gasparini, S. Feldmann, J. Wade, M.J. Fuchter, Chiral materials and mechanisms for circularly polarized light-emitting diodes, *Nat. Photonics* (2024) 1–11.
- [9] Z. Han, F. Wang, J. Sun, X. Wang, Z. Tang, Recent advances in ultrathin chiral metasurfaces by twisted stacking, *Adv. Mater.* 35 (3) (2023) 2206141.
- [10] Z. Wang, F. Cheng, T. Winsor, Y. Liu, Optical chiral metamaterials: a review of the fundamentals, fabrication methods and applications, *Nanotechnology* 27 (41) (2016) 412001.
- [11] J. Jiang, M. Chen, J.A. Fan, Deep neural networks for the evaluation and design of photonic devices, *Nat. Rev. Mater.* (2020) 1–22.
- [12] T. Tanaka, Y. Urabe, T. Hirakawa, H. Kataura, Simultaneous chirality and enantiomer separation of metallic single-wall carbon nanotubes by gel column chromatography, *Anal. Chem.* 87 (18) (2015) 9467–9472.
- [13] X. Wei, T. Tanaka, Y. Yomogida, N. Sato, R. Saito, H. Kataura, Experimental determination of excitonic band structures of single-walled carbon nanotubes using circular dichroism spectra, *Nature Commun.* 7 (2016) 12899.
- [14] X. Wei, T. Tanaka, T. Hirakawa, Y. Yomogida, H. Kataura, Determination of enantiomeric purity of single-wall carbon nanotubes using flavin mononucleotide, *J. Am. Chem. Soc.* 139 (45) (2017) 16068–16071.
- [15] X. Wei, T. Tanaka, T. Hirakawa, M. Tsuzuki, G. Wang, Y. Yomogida, A. Hirano, H. Kataura, High-yield and high-throughput single-chirality enantiomer separation of single-wall carbon nanotubes, *Carbon* 132 (2018) 1–7.
- [16] H. Li, G. Gordeev, O. Garrity, N.A. Peyyety, P.B. Selvasundaram, S. Dehm, R. Krupke, S. Cambré, W. Wenseleers, S. Reich, M. Zheng, J.A. Fagan, B.S. Flavel, Separation of specific single-enantiomer single-wall carbon nanotubes in the large-diameter regime, *ACS Nano* 14 (1) (2020) 948–963.
- [17] X. Wei, S. Li, W. Wang, X. Zhang, W. Zhou, S. Xie, H. Liu, Recent advances in structure separation of single-wall carbon nanotubes and their application in optics, electronics, and optoelectronics, *Adv. Sci.* (2022) 2200054.
- [18] X. He, W. Gao, L. Xie, B. Li, Q. Zhang, S. Lei, J.M. Robinson, E.H. Házó, S.K. Doorn, W. Wang, R. Vajtai, P.M. Ajayan, W.W. Adams, R.H. Hauge, J. Kono, Wafer-scale monodomain films of spontaneously aligned single-walled carbon nanotubes, *Nat. Nanotechnol.* 11 (7) (2016) 633–638.
- [19] W. Gao, J. Kono, Science and applications of wafer-scale crystalline carbon nanotube films prepared through controlled vacuum filtration, *R. Soc. Open Sci.* 6 (3) (2019) 181605.
- [20] J. Doumani, M. Lou, O. Dewey, N. Hong, J. Fan, A. Baydin, K. Zahn, Y. Yomogida, K. Yanagi, M. Pasquali, et al., Engineering chirality at wafer scale with ordered carbon nanotube architectures, *Nature Commun.* 14 (1) (2023) 7380.
- [21] J. Fan, R. Chen, M. Lou, H. Xie, N. Hong, Y. Tang, W. Gao, A programmable wafer-scale chiroptical heterostructure of twisted aligned carbon nanotubes and phase change materials, 2024, arXiv preprint arXiv:2406.13190.
- [22] R.B. Weisman, J. Kono, Handbook of Carbon Nanomaterials (Volumes 9–10), Vol. 9, World Scientific, 2019.
- [23] K. Momma, F. Izumi, Vesta 3 for three-dimensional visualization of crystal, volumetric and morphology data, *J. Appl. Crystallogr.* 44 (6) (2011) 1272–1276.
- [24] Y. Yomogida, T. Tanaka, M. Zhang, M. Yudasaka, X. Wei, H. Kataura, Industrial-scale separation of high-purity single-chirality single-wall carbon nanotubes for biological imaging, *Nature Commun.* 7 (2016) 12056.
- [25] Z. Wu, Z. Chen, X. Du, J.M. Logan, J. Sippel, M. Nikolou, K. Kamaras, J.R. Reynolds, D.B. Tanner, A.F. Hebard, et al., Transparent, conductive carbon nanotube films, *Science* 305 (5688) (2004) 1273–1276.
- [26] L. Zhao, J. Fan, C. Gong, A. Dyke, W. Gao, B. Li, A critical review on recent progress of solution-processed monolayer assembly of nanomaterials and applications, *Small* (2024) 2312268.
- [27] N. Sato, Y. Tatsumi, R. Saito, Circular dichroism of single-wall carbon nanotubes, *Phys. Rev. B* 95 (15) (2017) 155436.
- [28] I. Lindell, A. Sihvola, S. Tretyakov, A.J. Viitanen, *Electromagnetic Waves in Chiral and Bi-Isotropic Media*, Artech House, 1994.
- [29] H. Wu, T. Nishihara, A. Takakura, K. Matsuda, T. Tanaka, H. Kataura, Y. Miyauchi, Birefringent optical responses of single-chirality carbon nanotube membranes, *Carbon* 218 (2024) 118720.
- [30] E.U. Condon, Theories of optical rotatory power, *Rev. Modern Phys.* 9 (4) (1937) 432.
- [31] T.G. Mackay, A. Lakhtakia, *The Transfer-Matrix Method in Electromagnetics and Optics*, Springer Nature, 2022.
- [32] M. Wuttig, H. Bhaskaran, T. Taubner, Phase-change materials for non-volatile photonic applications, *Nat. Photonics* 11 (8) (2017) 465.
- [33] P. Guo, A.M. Sarangan, I. Agha, A review of germanium-antimony-telluride phase change materials for non-volatile memories and optical modulators, *Appl. Sci.* 9 (3) (2019) 530.
- [34] S. Abdollahramezani, O. Hemmatyar, H. Taghinejad, A. Krasnok, Y. Kiarashinejad, M. Zandehshahvar, A. Alù, A. Adibi, Tunable nanophotonics enabled by chalcogenide phase-change materials, *Nanophotonics* 1 (ahead-of-print) (2020).
- [35] Y. Zhang, C. Ríos, M.Y. Shalaginov, M. Li, A. Majumdar, T. Gu, J. Hu, Myths and truths about optical phase change materials: A perspective, *Appl. Phys. Lett.* 118 (21) (2021) 210501.
- [36] S. Raoux, G.W. Burr, M.J. Breitwisch, C.T. Rettner, Y.-C. Chen, R.M. Shelby, M. Salinga, D. Krebs, S.-H. Chen, H.-L. Lung, et al., Phase-change random access memory: A scalable technology, *IBM J. Res. Dev.* 52 (4.5) (2008) 465–479.
- [37] Q. Wang, E.T. Rogers, B. Gholipour, C.-M. Wang, G. Yuan, J. Teng, N.I. Zheludev, Optically reconfigurable metasurfaces and photonic devices based on phase change materials, *Nat. Photonics* 10 (1) (2016) 60–65.
- [38] Y. Wang, P. Landreman, D. Schoen, K. Okabe, A. Marshall, U. Celano, H.-S.P. Wong, J. Park, M.L. Brongersma, Electrical tuning of phase-change antennas and metasurfaces, *Nat. Nanotechnol.* (2021) 1–6.
- [39] Y. Zhang, C. Fowler, J. Liang, B. Azhar, M.Y. Shalaginov, S. Deckoff-Jones, S. An, J.B. Chou, C.M. Roberts, V. Liberman, et al., Electrically reconfigurable non-volatile metasurface using low-loss optical phase-change material, *Nat. Nanotechnol.* (2021) 661–666.
- [40] S. Abdollahramezani, O. Hemmatyar, M. Taghinejad, H. Taghinejad, A. Krasnok, A.A. Eftekhari, C. Teichrib, S. Deshmukh, M.A. El-Sayed, E. Pop, et al., Electrically driven reprogrammable phase-change metasurface reaching 80% efficiency, *Nature Commun.* 13 (1) (2022) Article number: 1696.
- [41] C. Ríos, M. Stegmaier, P. Hosseini, D. Wang, T. Scherer, C.D. Wright, H. Bhaskaran, W.H. Pernice, Integrated all-photonic non-volatile multi-level memory, *Nat. Photonics* 9 (11) (2015) 725–732.
- [42] Z. Cheng, C. Ríos, W.H. Pernice, C.D. Wright, H. Bhaskaran, On-chip photonic synapse, *Sci. Adv.* 3 (9) (2017) e1700160.
- [43] C. Ríos, N. Youngblood, Z. Cheng, M. Le Gallo, W.H. Pernice, C.D. Wright, A. Sebastian, H. Bhaskaran, In-memory computing on a photonic platform, *Sci. Adv.* 5 (2) (2019) eaau5759.
- [44] Y. Zhang, J.B. Chou, J. Li, H. Li, Q. Du, A. Yadav, S. Zhou, M.Y. Shalaginov, Z. Fang, H. Zhong, et al., Broadband transparent optical phase change materials for high-performance nonvolatile photonics, *Nature Commun.* 10 (2019) 4279.
- [45] Z. Fang, R. Chen, J. Zheng, A.I. Khan, K.M. Neilson, S.J. Geiger, D.M. Callahan, M.G. Moebius, A. Saxena, M.E. Chen, et al., Ultra-low-energy programmable non-volatile silicon photonics based on phase-change materials with graphene heaters, *Nat. Nanotechnol.* 17 (8) (2022) 842–848.
- [46] Y. Tang, P.T. Zamani, R. Chen, J. Ma, M. Qi, C. Yu, W. Gao, Device-system end-to-end design of photonic neuromorphic processor using reinforcement learning, *Laser Photonics Rev.* (2022) 2200381.